

A study on the energy transfer of a square prism under aeroelastic galloping

H.G.K.G. Jayatunga, B.T. Tan, J. S. Leontini

Abstract

Extracting useful energy from flow induced vibrations has become a developing area of research in recent years. In this paper, we analyse power transfer of an elastically mounted body under the influence of aeroelastic galloping. The system and the power transfer is analysed by numerically integrating the quasi-steady state model equations. The power transfer is analysed for both high ($Re = 22300$) and low ($Re = 165$) Reynolds numbers cases, and the impact of the system mass is investigated for both.

At high mass ratios ($m^* > 50$), the power transfer is completely controlled by galloping and essentially independent of the mass. A combined mass-damping coefficient, Π_2 , that can be derived from the equation of motion, is shown to be the parameter that governs power output. The system is a balance between the power delivered to the system due to hydrodynamic forcing and power removed through mechanical damping which are governed by the hydrodynamic forcing characteristics (i.e. the lift force as a function of incident angle) and mechanical damping coefficient respectively. The peak efficiency of 0.26% for $Re = 165$ and 6.7% for $Re = 22300$ were observed when the non-dimensionalised mass-damping factor becomes 0.314 and 1.04 respectively.

A contradictory behaviour is observed at low m^* between the low and high Re cases. The forcing due to vortex shedding at low Reynolds numbers suppresses the galloping excitation and results in a reduced power output. For the case with high Re power output increases as m^* is reduced. For this high Re case, at low m^* the reduction in inertia allows the body to accelerate faster and spend a larger portion of the period at relatively high transverse velocities. Extrapolating this trend, the limit to peak efficiency is found to be 13.5% and occurs when $m^* \rightarrow 0$ and $U^* \rightarrow \infty$ and $\Pi_2 = 1.22$

Keywords:

1. Introduction

The search for alternate energy sources with minimal environmental impact has become an important area of research in the modern world. Solar, wind power and wave power are some of the examples of these sources. Recently, a new branch of research has been developing to extract energy from flow induced vibrations (Bernitsas et al., 2008). It has been hypothesized that this technique may work efficiently in areas where regular turbines cannot.

An elastically-mounted slender structure such as a cylinder which is susceptible to flow-induced vibrations has the potential for energy extraction. With regards to slender bodies, two common types of flow-induced vibrations are vortex-induced vibrations (VIV) and aeroelastic galloping. Significant research has been carried out by Bernitsas and his team on extracting useful energy from VIV. Some of their significant work includes investigating the influence of physical parameters such as mass ratio, Reynolds number, mechanical properties (Raghavan and Bernitsas, 2011; Lee and Bernitsas, 2011) and the influence of the proximity of a solid boundary (Raghavan et al., 2009). However, the possibility of extracting energy using aeroelastic galloping has not been thoroughly investigated. Some theoretical work was carried out by Barrero-Gil et al. (2010). Utilizing galloping may be a more viable method to harness energy from flow-induced vibrations as it is not bounded by a narrow “lock-in” range of reduced velocities (U^*). This study further explores the possibility of harnessing energy from flow induced vibrations using aeroelastic galloping.

According to Païdoussis et al. (2010), Glauert (1919) provided a criterion for galloping by considering the auto-rotation of an aerofoil. Den Hartog (1956) provided a theoretical explanation for galloping for iced electric transmission lines. A weakly non-linear theoretical aeroelastic model to predict the response of galloping was developed by Parkinson and Smith (1964) based on the quasi-steady state (QSS) theory. Experimental lift and drag data on a fixed square prism at different angles of attack were used as an input for the theoretical model. It essentially used a curve fit of the transverse force to predict the galloping response. The study managed to achieve a good agreement with experimental data.

However, the QSS model equation when solved analytically using the sinusoidal solution method cannot predict the response for cases with low mass ratios. Joly et al. (2012) observed that finite element simulations show a sudden change in amplitude below a critical value of the mass ratio. The model equation defined in Parkinson and Smith (1964) was modified to account for the vortex shedding and solved numerically to predict the reduced amplitude at low mass ratios to the point where galloping is no longer present. Barrero-Gil et al. (2010) investigated the possibility of extracting power from vibrations caused by galloping using the quasi-steady state model. In the conclusions of that paper it was pointed out that in order to obtain a high power to area ratio, the mass-damping ($m^*\zeta$) parameter should be kept low. The same study investigated the influence of the characteristics of the C_y curve on maximum power output.

Here, the modified QSS model developed by Joly et al. (2012) is integrated numerically for low Reynolds numbers. The focus is on the power extraction potential as a function of mechanical parameters (i.e. frequency of oscillation, damping factor and mass ratio). To this end, a series of previously mentioned mechanical parameters are tested at two different values of Re : $Re = 165$, a case that should remain laminar and essentially two-dimensional; $Re = 22300$, a case where the flow is expected to be turbulent and three-dimensional. Both cases require the input of transverse force coefficients C_y as a function of angle of attack θ for a fixed body. These data are provided from direct numerical simulations for the $Re = 165$ case, while the data provided by Parkinson and Smith (1964) are used for the $Re = 22300$ case.

The structure of the paper is as follows. Section 2 presents the modified QSS model, the method for the calculation of power output, and the parameters used. Section 3 presents the results, first of the fixed body tests at a range of θ , then of the response characteristics predicted by the integration of the QSS model for both the high and low Re cases. For the low Re case, the results of the QSS model are compared to those of full direct numerical simulations of the fluid-structure interaction problem. Finally, section 4 presents the conclusions that can be drawn from this work.

Nomenclature

a_1, a_3, a_5, a_7	coefficients of the polynomial to determine C_y
A	displacement amplitude
c	damping constant
D	characteristic length (side length) of the cross section of the body
$f = \sqrt{k/m}/2\pi$	natural frequency of the system
F_y	instantaneous force normal to the flow
F_0	amplitude of the oscillatory force due to vortex shedding
k	spring constant
m	mass of the body
m_a	added mass
P_d	power dissipated due to mechanical damping
$P_{in} = \rho U^3 D/2$	Energy flux of the approaching flow
P_{mean}	mean power
P_t	power transferred to the body by the fluid
t	time
U	freestream velocity
U_i	Induced velocity
y, \dot{y}, \ddot{y}	transverse displacement, velocity and acceleration of the body
$\mathcal{A} = DL$	frontal area of the body
λ	Inverse time scale of a galloping dominated flow
$\lambda_{1,2}$	Eigenvalues of linearized equation of motion
ρ	fluid density
$\omega_n = 2\pi f$	natural angular frequency of the system
ω_s	vortex shedding angular frequency
$c^* = cD/mU$	non-dimensionalised damping factor
$C_y = F_y/0.5\rho U^2 DL$	normal (lift) force coefficient
$m^* = m/\rho D^2 L$	mass ratio
Re	Reynolds number
$U^* = U/fD$	reduced velocity
$Y = y/D$	non-dimensional transverse displacement
$\dot{Y} = m^* \dot{y}/a_1 U$	non-dimensional transverse velocity
$\ddot{Y} = m^{*2} D/a_1^2 U^2$	non-dimensional transverse acceleration
$\Gamma_1 = 4\pi^2 m^{*2}/U^{*2} a_1^2$	First dimensionless group arising from linearised, non-dimensionalised equation
$\Gamma_2 = c^* m^*/a_1$	Second dimensionless group arising from linearised, non-dimensionalised equation
$\zeta = c/2m\omega_n$	damping ratio
$\theta = \tan^{-1}(\dot{y}/U)$	instantaneous angle of incidence (angle of attack)
$\Pi_1 = 4\pi^2 m^{*2}/U^{*2}$	Combined mass-stiffness parameter
$\Pi_2 = c^* m^*$	Combined mass-damping parameter

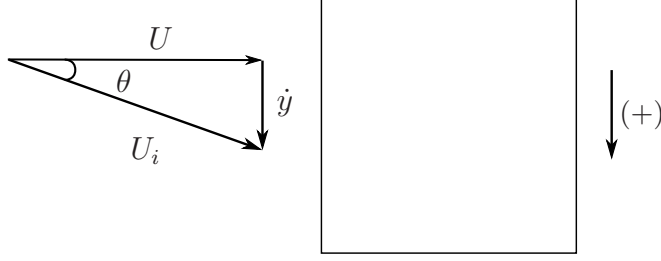


Figure 1: Induced angle of attack on the square prism due to the resultant of free-stream velocity of the fluid and transverse velocity of the body.

2. Problem formulation and methodology

2.1. The quasi-steady state (QSS) model

The base quasi-steady state (QSS) model was first developed by Parkinson and Smith (1964) for a square cross section. The equation of motion of the body is given by

$$(m + m_a)\ddot{y} + c\dot{y} + ky = F_y, \quad (1)$$

where the forcing term F_y is given by

$$F_y = \frac{1}{2}\rho U^2 \mathcal{A} C_y. \quad (2)$$

Lighthill (1986) showed that for systems oscillating in fluid, it is sometimes useful to decompose the fluid forces into components that are in and out of phase with the body acceleration. The component in phase with the acceleration effectively adds to the inertia or effective mass of the system. Therefore, an added mass term, m_a , can be added to the system mass. For consistency with previous studies such as Joly et al. (2012), a value of $m_a = 3.5$ has been used here.

In the QSS model, it is assumed that the force on the body at a given instantaneous incident angle θ (defined in figure 1) is the same as the mean force on a static body at the same incident angle, or angle of attack. The instantaneous value of C_y is therefore determined by an interpolating polynomial based on the lift data for flow over a stationary body at various θ . Using the relationship between θ and the instantaneous transverse velocity of the body \dot{y} shown in figure 1, C_y can be written as a function of \dot{y} . The order of the interpolation polynomial used to define this function has varied from study to study. For example a 7th order polynomial was used in Parkinson and Smith (1964) and 3rd order polynomial was used in Barrero-Gil et al. (2009). Ng et al. (2005) concluded that using a 7th order polynomial is sufficient and a polynomial higher than that of 7th order doesn't provides a significantly better result. Thus a 7th order interpolating polynomial is used in this present study. As a result, $C_y(\theta)$ (noting that theta is proportional to \dot{y}/U) is defined as

$$C_y(\theta) = a_1 \left(\frac{\dot{y}}{U} \right) + a_3 \left(\frac{\dot{y}}{U} \right)^3 + a_5 \left(\frac{\dot{y}}{U} \right)^5 + a_7 \left(\frac{\dot{y}}{U} \right)^7. \quad (3)$$

It is expected that vortex shedding will be well correlated along the span and provide significant forcing at low Re . Joly et al. (2012) introduced an additional sinusoidal forcing function to the hydrodynamic forcing to model this. This enables the model to provide accurate predictions even at low mass ratios where galloping excitation is suppressed or not present. In this study, the forcing due to vortex shedding in low Re cases is incorporated using a sinusoidal forcing function $F_0 \sin \omega_s t$ added to the right-hand side of equation 1. Here, ω_s and F_0 represent the angular vortex shedding frequency and the maximum force due to shedding respectively. Thus, the final equation for the modified QSS model is

$$m\ddot{y} + c\dot{y} + ky = \frac{1}{2}\rho U^2 \mathcal{A} \left(a_1 \left(\frac{\dot{y}}{U} \right) + a_3 \left(\frac{\dot{y}}{U} \right)^3 + a_5 \left(\frac{\dot{y}}{U} \right)^5 + a_7 \left(\frac{\dot{y}}{U} \right)^7 \right) + F_0 \sin(\omega_s t). \quad (4)$$

This equation can be solved using standard time integration methods. In this study the fourth-order Runge-Kutta scheme built in to the MATLAB routine ‘ode45’ was generally used to obtain the solutions. Some low mass ratio cases used a solver modified for stiff problems, built into the ‘ode15s’ routine in MATLAB.

2.2. Calculation of average power

The dissipated power due to the mechanical damping represents the ideal potential amount of harvested power output. Therefore, the mean power output can be given by

$$P_{mean} = \frac{1}{T} \int_0^T (c\dot{y})\dot{y}dt, \quad (5)$$

where T is the period of integration and c is the mechanical damping constant.

It should be noted that this quantity is equal to the work done on the body by the fluid, defined as

$$P_{mean} = \frac{1}{T} \int_0^T F_y \dot{y}dt, \quad (6)$$

where F_y is the transverse (lift) force.

These two definitions show two important interpretations of the power with respect to any energy production device. The first shows that power will be high for situations where the damping coefficient is high, and the transverse velocity is consistently high. The second shows that power will be high for situations where the transverse force and the body velocity are in phase.

2.3. Parameters used

For the low Re tests, $Re = 165$ was maintained as it was pointed out by Sheard et al. (2009) and Tong et al. (2008) that the three-dimensional transition for a square cylinder occurs at approximately $Re=160$. F_0 was kept at 0.4937 which was obtained by scaling the value used by Joly et al. (2012) with the amplitude ratios of the lift forces obtained at the different Reynolds numbers.

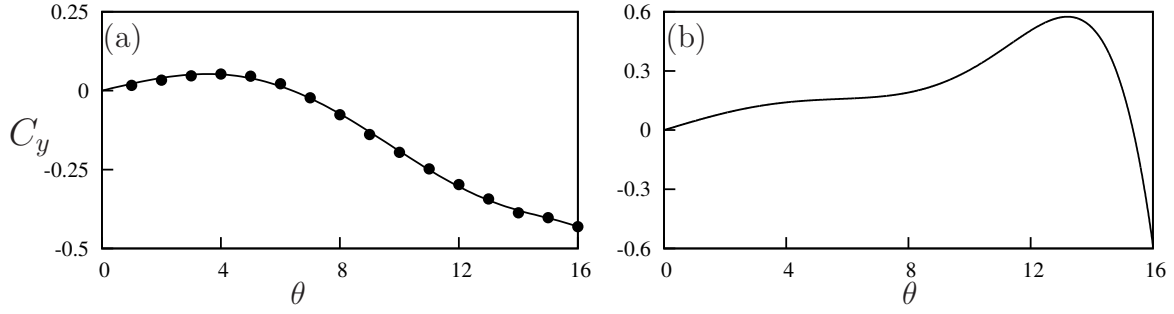


Figure 2: Lift coefficient, C_y , as a function of incidence angle θ , for a static square cross section. (a) Data from simulations at $Re = 165$ (b) data from Parkinson and Smith (1964) at $Re = 22300$. Points (\bullet) are measurements from the simulations. The solid lines in both plots are 7th-order interpolating polynomial used to predict the fluid forcing for the QSS model. C_y is the force coefficient of the force which occurs normal to the induced velocity.

Case	a_1	a_3	a_5	a_7
Re=165	1.3	125.3	1825.73	8765.3
Re=22300	2.69	168	1670	59900

Table 1: Coefficient values used in the 7th order interpolation polynomial for high ($Re = 22300$) and low ($Re = 165$) Reynolds numbers. These data are used as input data to calculate the right-hand side of Eq. 4 throughout this study.

The angular vortex shedding frequency ω_s , was set to 0.98 which was obtained by performing a power spectral analysis of the stationary data at 0° . Stationary C_y data were obtained at different angles of attack ranging from 0° to 16° . The average power was obtained by using equation 5, and the averaging was done over no less than 20 galloping periods. Predictions of power output at $Re = 22300$ were obtained using the coefficients for curve fitting C_y (Table (1)) from Parkinson and Smith (1964), in order to provide a comparison between high and low Reynolds numbers. The mass ratio m^* was kept at 1163 for $Re = 22300$ (Similar to Parkinson and Smith (1964)) and $m^* = 20$ for $Re=165$. These parameters were used throughout this study unless otherwise specified.

The stationary data and the fluid-structure interaction (FSI) data were obtained using a high-order spectral element routine to simulate the two-dimensional laminar flow. Simulations involving fluid structure interaction (FSI) were used to provide additional validation of the QSS model. The inlet was placed $20D$ while the outlet situated $60D$ away from the centroid of the body. The side boundaries were placed $20D$ away from the centroid of the body where D was kept as unity throughout this study. The Navier–Stokes equations were solved in an accelerated frame of reference attached to the moving body along with the body equation of motion given in equation 1. A three-step time splitting scheme together

with high-order Lagrangian polynomials were used to obtain the solution. The details of the method can be found in Thompson et al. (2006, 1996). This code has been very well validated in a variety of fluid-structure interaction problems (Leontini et al., 2007; Griffith et al., 2011; Leontini et al., 2011; Leontini and Thompson, 2013).

The computational domain consists of 690 quadrilateral macro elements where the majority of the elements were concentrated near the square section. A freestream condition was given to the inlet, top and bottom boundaries and the normal velocity gradient was set to zero at the outlet. A convergence study was performed by changing the order of the polynomial (p -refinement) at $U^* = 40$ and $Re = 165$. A 9th order polynomial together with a time step of $\Delta t U/D = 0.001$ was sufficient to ensure an accuracy of 2% with regards to amplitude of oscillation.

3. Results

3.1. Stationary data

The characteristic lift force data for a stationary body (C_y) as a function of incident angle θ obtained using flow simulations are shown in figure 3(a). They agree well with the low Re data presented in Joly et al. (2012).

However, there are several differences that can be observed when the low Re data are compared with the 7th order polynomial curve at $Re = 22300$ shown in figure 3(b). The peak value of C_y is significantly lower at $Re = 165$ ($C_y = 0.05$ at 4°) in comparison with $Re = 22300$ ($C_y = 0.57$ at 13°). The inflection point present around 8° for $Re = 22300$ is not observed at $Re = 165$. This agrees with the findings of Luo et al. (2003).

It was concluded by Luo et al. (2003) that hysteresis in the system response occurs due to the inflection point in the C_y curve. Therefore hysteresis is not expected at $Re = 165$.

The range of incident flow angles where C_y remains positive is narrow at $Re = 165$ ($0^\circ < \theta \leq 6^\circ$) compared to $Re = 22300$ ($0^\circ < \theta \leq 15^\circ$). This feature is what sustains galloping. Power is only transferred from the fluid to the supporting structure within this range of incident angles because fluid forces are acting in the direction of travel of the oscillating body, as demonstrated by equation 6. Incident angles beyond this range actually suppress the galloping and power goes in the opposite direction, i.e; from body to fluid. Therefore due to the overall smaller C_y and narrow range of angles where C_y is positive for $Re = 165$ compared to $Re = 22300$, it is expected that power output at $Re = 165$ is significantly lower than at $Re = 22300$.

3.2. Displacement, velocity and power output as a function of reduced velocity

The quasi-steady analysis data reveal that the displacement amplitude grows with increasing U^* . This is shown for both the high and low Re cases in figures 3 (a) and (b). The onset of galloping is delayed with increasing damping ratio ζ for both high and low Reynolds numbers. This echos the findings of previous studies by Parkinson and Smith (1964) and Barrero-Gil et al. (2010). Hysteresis could be observed for the case with a higher Reynolds number. Different solutions could be obtained by manipulating the initial conditions (initial displacement) of the system. The upper branch was obtained

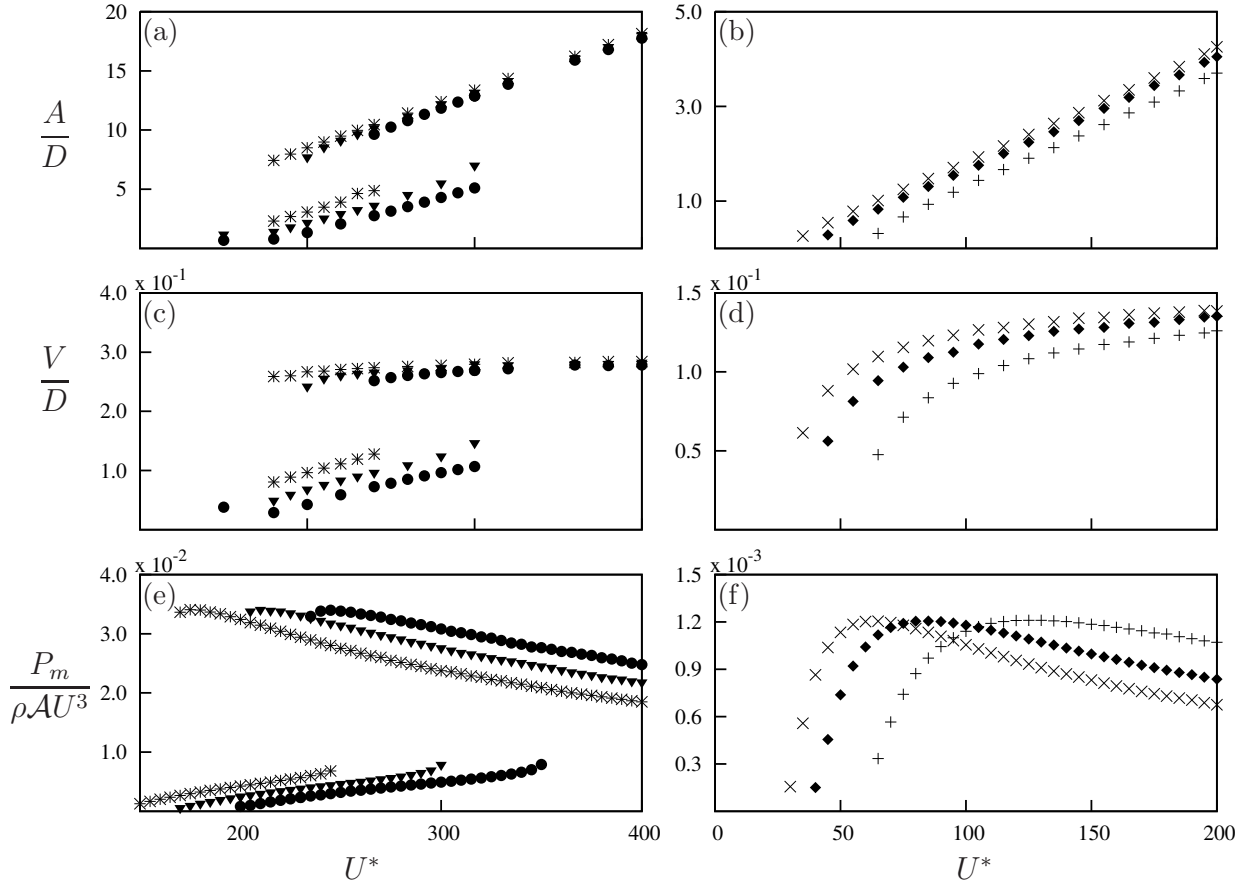


Figure 3: Velocity amplitude, displacement amplitude and mean power as functions of U^* . Data presented in (a), (c) and (e) were calculated using input data at $Re = 22300$ and $m^* = 1163$ obtained by Parkinson and Smith (1964) at three different damping ratios: $\zeta = 0.0125$ (*), $\zeta = 0.015$ (▼) and $\zeta = 0.0175$ (●). Data presented in (b),(d) and (f) were obtained using input data at $Re = 165$ and $m^* = 20$ at three different damping ratios: $\zeta = 0.075$ (×), $\zeta = 0.1$ (◆) and $\zeta = 0.15$ (+). The multiple branches for the higher Re are due to the hysteresis between two solutions.

by giving an initial displacement which was higher than the expected amplitude while the lower branch was obtained by providing a lower initial displacement than the expected amplitude. Although theory shows a possible third state, it is an unstable branch and as such it could not be achieved numerically. This was also observed by Vio et al. (2007).

*Power vs U^**

The mean power grows, peaks and then slightly reduces as the reduced velocity U^* is increased. This is shown in figure 3(e) and (f) for each value of ζ . The value of U^* at which the peak power occurs increases with ζ . However, the magnitude of the peaks remain constant for all the values of ζ . Barrero-Gil et al. (2010) also observed a similar behaviour. The higher Reynolds number case clearly shows hysteresis in the power data. The range of hysteresis increases with increasing ζ .

Unlike VIV, which is a resonant-type phenomenon, the quasi-steady system describing galloping has no strongly preferred frequency. Although the onset of galloping and the value of U^* where peak power occurs varies with the damping ratio ζ , the power extracted remains almost constant for values of U^* beyond that where the peak power occurs.

The efficiency of the system can be defined as the ratio of the time average power output to $P_{in} = \rho U^3 D/2$, the kinetic energy in the fluid approaching the body. A similar definition was given in Barrero-Gil et al. (2010)). The current results show that the system has a peak efficiency of 0.26% for $Re = 165$ and 6.7% for $Re = 22300$. The peak efficiency reported in Barrero-Gil et al. (2010) for $Re = 22300$ is approximately 5% less than the current result. This difference is due to Barrero-Gil et al. (2010) using a 3^{rd} order polynomial as the interpolating polynomial which under predicts the forcing at values of θ where the maximum force occurs as compared to the 7^{th} order polynomial used in this study.

3.3. Galloping response and governing parameters

The data presented in figure 3 show that, regardless of the damping ratio ζ , the trend of the response with U^* is similar, suggesting the data can be collapsed by a suitable choice of parameters. These parameters can be found by considering the natural time scales of the equations of motion presented in equation 4, and by suitably non-dimensionalizing these equations.

The natural time scales of the system can be found by solving for the eigenvalues of the linearized equation of motion, namely

$$(m + m_a)\ddot{y} + c\dot{y} + ky = \frac{1}{2}\rho U^2 \mathcal{A}a_1 \left(\frac{\dot{y}}{U} \right), \quad (7)$$

which is simply the equation of motion presented in equation 4 with the polynomial series for the lift force truncated at the linear term, and the forcing term representing vortex shedding removed.

Combining the \dot{y} terms and solving for eigenvalues gives

$$\lambda_{1,2} = -\frac{1}{2} \frac{c - \frac{1}{2}\rho U \mathcal{A}a_1}{(m + m_a)} \pm \frac{1}{2} \sqrt{\left[\frac{c - \frac{1}{2}\rho U \mathcal{A}a_1}{(m + m_a)} \right]^2 - 4 \frac{k}{(m + m_a)}}. \quad (8)$$

If it is assumed that the spring is relatively weak, $k \rightarrow 0$, a single non-zero eigenvalue remains. This eigenvalue is

$$\lambda = -\frac{c - \frac{1}{2}\rho U \mathcal{A} a_1}{(m + m_a)}. \quad (9)$$

Further, if it is assumed that the mechanical damping is significantly weaker than the aerodynamic forces on the body, $c \rightarrow 0$ and

$$\lambda = \frac{\frac{1}{2}\rho U \mathcal{A} a_1}{(m + m_a)}. \quad (10)$$

For reasonably heavy bodies, the impact of the added mass can also be neglected, to arrive at a definition of λ as

$$\lambda = \frac{\frac{1}{2}\rho U \mathcal{A} a_1}{m}. \quad (11)$$

In this form, λ represents the inverse time scale of the motion of the body due to the negative damping effect of the long-time aerodynamic forces. In fact, the terms can be regrouped and λ written as

$$\lambda = \frac{a_1}{m^*} \frac{U}{D} \quad (12)$$

Written this way, the important parameters that dictate this inverse time scale are clear. The rate of change in the aerodynamic force with respect to angle of attack when the body is at the equilibrium position, $\partial C_y / \partial \alpha$, is represented by a_1 . The mass ratio is represented by m^* . The inverse advective time scale of the incoming flow is represented by the ratio U/D . Increasing a_1 would mean the force on the body would increase more rapidly with small changes in the angle of attack, θ , or transverse velocity. Equation 12 shows that such a change will increase the inverse time scale, or analogously decrease the response time of the body. Increasing the mass of the body, thereby increasing m^* , has the opposite effect. The inverse time scale is decreased, or as might be expected, a heavier body will take longer to respond.

This timescale can then be used to non-dimensionalize the equation of motion, and to find the relevant dimensionless groups of the problem. If the non-dimensional time, τ , is defined such that $\tau = t(a_1/m^*)(U/D)$, the equation of motion presented in equation 4 can be non-dimensionalized as

$$\ddot{Y} + \frac{m^{*2}}{a_1^2} \frac{kD^2}{mU^2} Y = \left(\frac{1}{2} - \frac{m^*}{a_1} \frac{cD}{mU} \right) \dot{Y} + H.O.T., \quad (13)$$

where $H.O.T.$ represents the higher order terms in \dot{Y} . The coefficients can be regrouped into combinations of non-dimensional groups, and rewritten as

$$\ddot{Y} + \frac{4\pi^2 m^{*2}}{U^{*2} a_1^2} Y = \left(\frac{1}{2} - \frac{c^* m^*}{a_1} \right) \dot{Y} + H.O.T, \quad (14)$$

where $c^* = cD/mU$ is a non-dimensional damping parameter.

Equation 14 shows there are four non-dimensional parameters that play a role in setting the response of the system. These are the stiffness (represented by the reduced velocity U^*), the damping c^* , the mass ratio m^* , and the geometry, represented by the rate of change in the aerodynamic force with respect to angle of attack when the body is at the equilibrium position, a_1 . The grouping of these parameters into two groups in equation 14 which arise by non-dimensionalising using the natural time scale of the galloping system, suggests there are two groups that dictate the response: $\Gamma_1 = 4\pi^2 m^{*2}/U^{*2} a_1^2$ and $\Gamma_2 = c^* m^*/a_1$. For a given geometry and Reynolds number, Γ_1 can be thought of as a combined mass-stiffness, whereas Γ_2 can be thought of as a combined mass-damping parameter. As it is assumed that during galloping the stiffness plays only a minor role, Γ_2 seems a likely parameter to collapse the data presented in figure 3. In fact, in the classic paper on galloping from Parkinson and Smith (1964), galloping data from wind tunnel tests is presented in terms of a parameter that can be shown to be the same as Γ_2 .

All of the quantities that make up Γ_1 and Γ_2 can, in theory, be known before an experiment is conducted. However, the quantity a_1 is a relatively difficult one to determine, requiring static body experiments or simulations. Here, the geometry is unchanged and results are only being compared at the same Re . Hence, suitable parameters can be formed by multiplying Γ_1 and Γ_2 by a_1^2 and a_1 respectively, to arrive at a mass-stiffness parameter $\Pi_1 = 4\pi^2 m^{*2}/U^{*2}$, and a mass-damping parameter defined as $\Pi_2 = c^* m^*$.

Figure 4 presents the same data as shown in figure 3, but in terms of the parameter Π_2 . The collapse, especially of the velocity amplitude and power output data, is excellent. This result shows that it is possible to obtain a similar power output at different values of U^* or ζ when the mass-damping constant, Π_2 , is kept fixed. An example of this is shown in figure 5, where the time history of two cases with clearly different U^* and ζ values, but the same value of $\Pi_2 = 0.3$, are plotted. The figure clearly shows that the common power output is a result of similar velocity amplitudes between cases if one were to disregard the high frequencies due to shedding.

Power can be expressed as the product of force and velocity. Therefore the instantaneous power from the fluid to the body can be expressed as $P_t = F_y \dot{y}$. Similarly the dissipated power due to the mechanical damping can be expressed as $P_d = (c\dot{y})\dot{y}$. The time average of these two quantities, described in equations 5 and 6 should be equal due to energy conservation, provided that the mechanical friction losses are neglected. The mean power vs U^* provides a detailed explanation for the variation of the output power when the reduced velocity is increased. The key regions consists of region 1 where the P_{mean} increases with U^* , region 2 where P_{mean} becomes maximum and region 3 where P_{mean} decreases with U^* . Time histories of P_t and P_d at each of these key regions are presented in figure 7.

The non-dimensional damping, c^* , can be shown to be inversely proportional to U^* . Hence the damping parameter, and the mass-damping Π_2 , reduces when moving from region 1 to 3. Figure 2(a) shows that C_y and therefore instantaneous force rises until 4° where it peaks and then falls, and at around 6° becomes negative. The maximum amount of power that can be transferred occurs when \dot{y} is such that θ is near the peak region. At the region where the instantaneous force becomes negative it will be opposing the velocity \dot{y} . Data

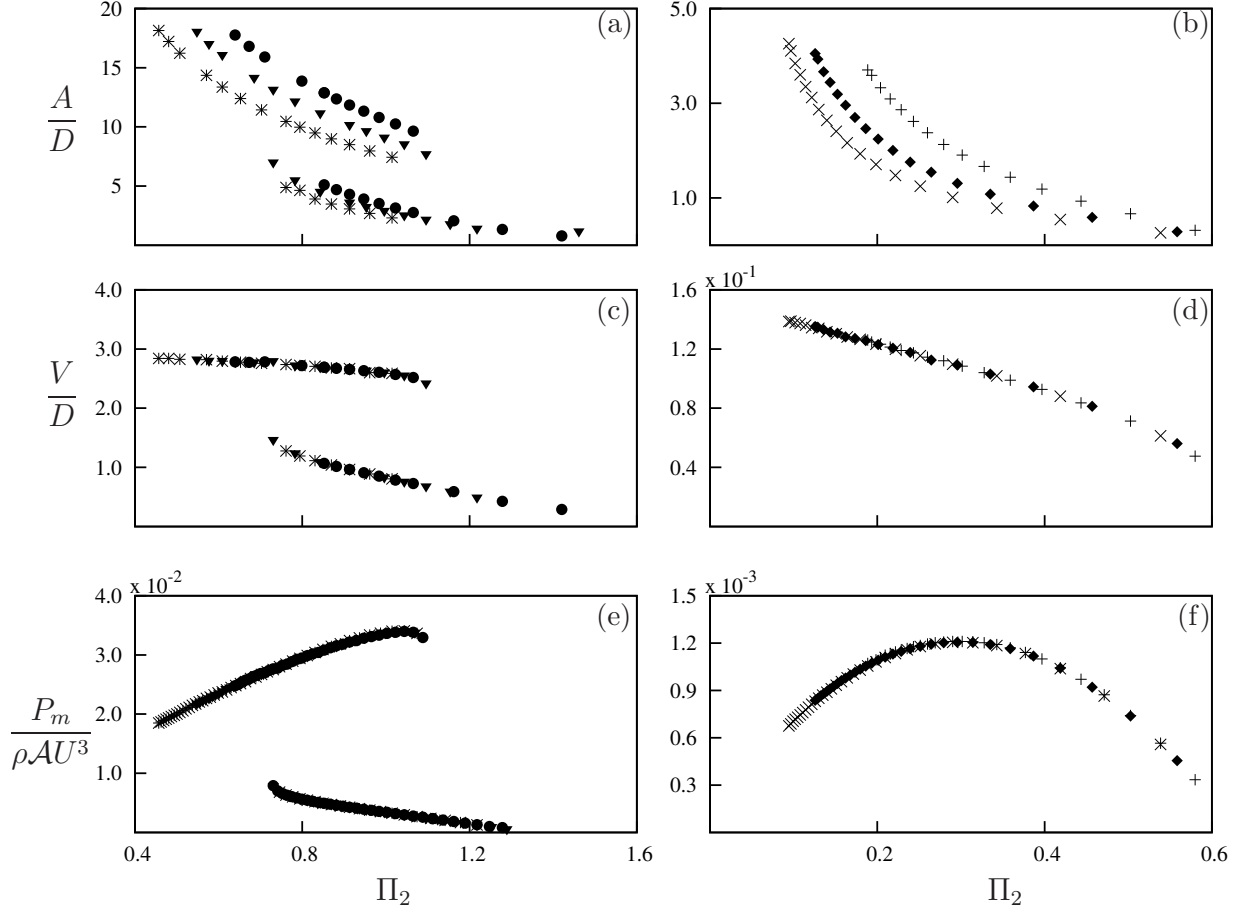


Figure 4: Displacement amplitude, velocity amplitude and mean power as functions of the mass-damping Π_2 . Data presented in (a),(c) and (e) were calculated using input data at $Re = 22300$ obtained by Parkinson and Smith (1964) at three different damping ratios: $\zeta = 0.0125$ (*), $\zeta = 0.015$ (▼) and $\zeta = 0.0175$ (●). Data presented in (b), (d) and (f) were obtained using input data at $Re = 165$ at three different damping ratios: $\zeta = 0.075$ (×), $\zeta = 0.1$ (◆) and $\zeta = 0.15$ (+). The collapsed data implies that there is no frequency selection and the tuning parameter of the mechanical side of the system is the damping constant to obtain an optimum power output.

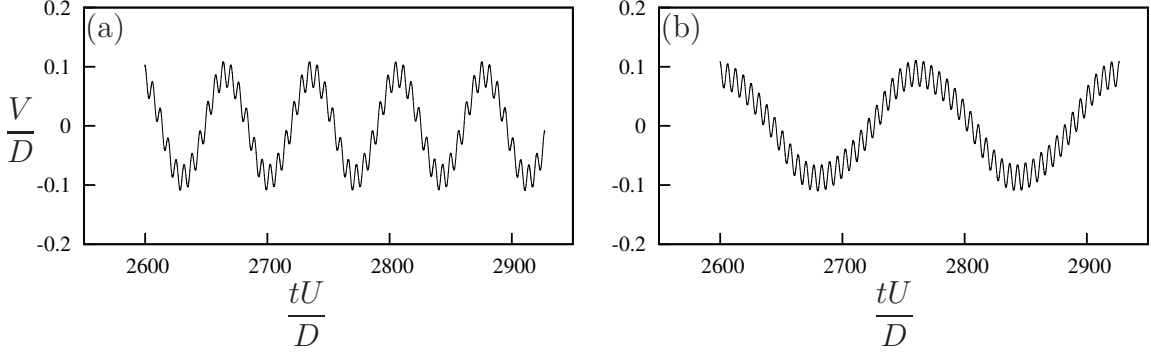


Figure 5: Time histories of velocity at two different ζ and U^* at $m^* = 20$ which produce the same mean power (1.2×10^{-3}). Data presented in (a) are at $U^* = 65$, $\zeta = 0.075$ and (b) are at $U^* = 150$, $\zeta = 0.175$. Both data sets were obtained using the QSS model using input C_y parameters at $Re = 165$. Shedding is evident in both signals as a high frequency fluctuation but the amplitude of the slower fluctuations remains constant in both cases.²

at $\zeta = 0.1$, $m^* = 40$ and $Re = 165$ are shown in figure 7 and are analysed as an example.

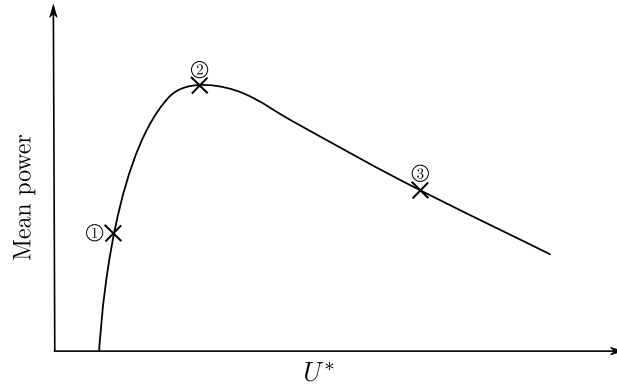


Figure 6: Three key regions taken into account to analyse the time histories of power in a typical mean power vs. U^* curve at $Re = 165$. In region 1, high damping suppresses oscillation, hence the power output is low. In region 2, the damping is close to the optimum for power transfer. In region 3, the low damping means little energy is extracted from the fluid.

At region 1 where $U^* = 90$, $\Pi_2 = 0.56$ the damping constant is high and a clear sinusoidal signal is observed for both P_d and P_t in figure 7(a). Figures 7(d) and 7(g) show that equivalent incident angle θ (which for small values, is proportional to the transverse velocity of the body) is in phase with F_y . The velocity amplitude in this case is small and θ is within the range where the hydrodynamic force increases with the incident angle (i.e. $0 < \theta \leq 4^\circ$ as shown in figure 2(a)). According to equation 6, these conditions are suitable for high power output. However in this case, the power output is limited by the high damping which limits the amplitude of the oscillation.

At region 3 ($U^* = 400$, $\Pi_2 = 0.13$) the damping is low in comparison with region 1 and 2. While this may lead to larger oscillations, damping is required to dissipate power

according to equation 5. Therefore, the low damping in this region leads to a low mean power output. Fig.7 (c) shows that P_t becomes negative over some portion of the cycle. This is caused by the high velocity amplitude leading to the equivalent incident angle θ to exceed the range where C_y is positive (i.e. $0 < \theta < 6^\circ$ as shown in figure 3(a)). In this portion of the cycle the hydrodynamic force actually opposes the direction of travel and power is transferred from the structure to the fluid during those times. From an energy perspective, the mechanical damping is not sufficient to remove the energy transferred from the fluid to the structure during other times of the cycle because Γ_2 is substantially low. Therefore this excess energy is transferred back to the fluid as depicted by the negative region of P_d in Fig.7(c).

At region 2 ($U^* = 165$, $\Pi_2 = 0.3$), a balance is found between high and low values of damping. P_t is not a pure sinusoidal signal, however the signal remains periodic. From the time history graph of P_t , two ‘peaks’ are present in a single half cycle as shown in figure 7(b). In this case, the velocity amplitude actually exceeds the equivalent incident angle where the hydrodynamic forces peaks (i.e. $\theta = 4^\circ$ in 3 (a)). The dips in P_d between the two peaks approximately correspond to the time where the transverse velocity is higher than 0.07 and F_y is decreasing with increasing transverse velocity. The mean power output is at its maximum. This is due to the fact that this region is the best compromise between region 1 and 3. The damping is high enough to obtain a high power output while not too high to allow the induced angle of attack to enter the region where the forcing opposes the direction of travel.

3.4. Effect of m^*

The mean power at different m^* is presented as a function of the mass-damping parameter Π_2 in figure 8(a) for the low Re case. For $m^* > 30$, the power output is essentially independent of m^* , while at $m^* \leq 30$, the power output reduces with reducing m^* across the parameter range. However, when the sinusoidal forcing function in equation 1, which caters for the vortex shedding, is disregarded, the reduction in power is not observed as shown in figure 8(b). The suppression of galloping response at low m^* and low Re due to the presence of vortex shedding has previously been observed by Joly et al. (2012). This is a non-linear interaction between the forcing that drives the galloping excitation and the forcing as a result of vortex shedding. The forcing associated with vortex shedding is significantly larger and at a higher frequency than the forcing that drives galloping. Systems with low m^* do not have enough inertia to fully sustain the galloping excitation over the longer period.

At $Re = 22300$ power output increases with decreasing m^* for cases with $m^* < 50$. The overall mean power tend to increase as the m^* was decreased when U^* was kept constant (Fig9 (a)). The same effect was observed when U^* was increased keeping m^* constant (9 (b)). It should be noted that the influence of U^* was observed only for low mass ratios. This is perhaps not surprising, as the definition of Π_1 shows that this mass-stiffness parameter goes quickly to zero as U^* grows, but that it will be of comparable order to the mass-damping Π_2 when U^* approaches unity. Therefore, the influence of this second parameter

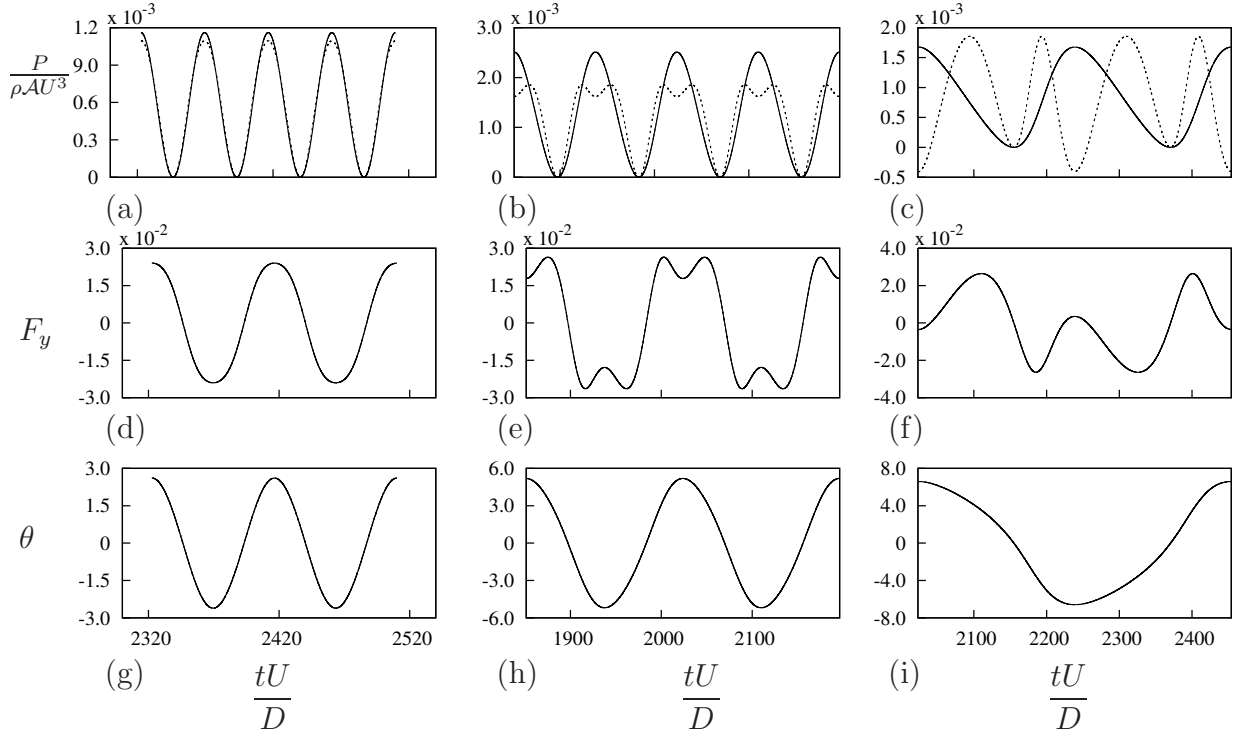


Figure 7: Time histories of P_t , P_d , F_y and θ at $U^* = 90, 165$ and 400 . Data was obtained at $\zeta = 0.1$, $m^* = 40$ and $Re=165$. The time histories of P_t (—) and P_d (---) are presented for: (a) $U^* = 90$; (b) $U^* = 165$; (c) $U^* = 400$. Time histories of the instantaneous force F_y for: (d) $U^* = 90$; (e) $U^* = 165$; (f) $U^* = 400$. Time histories of the instantaneous angle θ for: (g) $U^* = 90$; (h) $U^* = 165$; (i) $U^* = 400$.

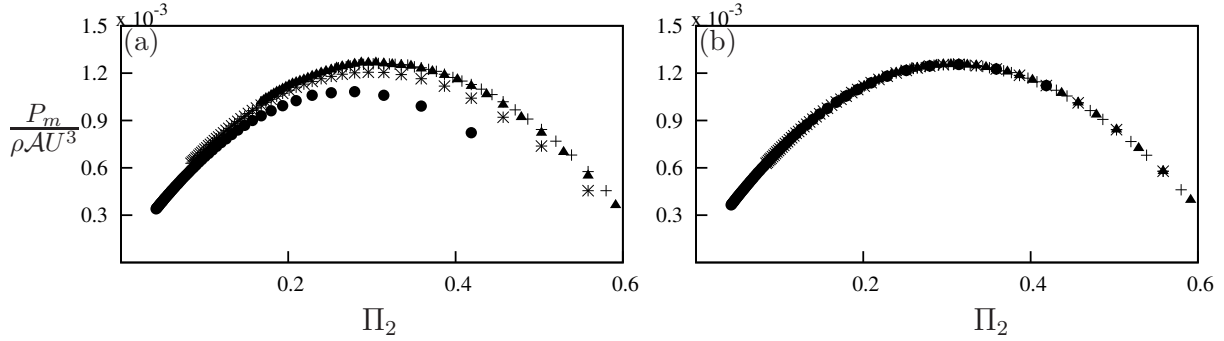


Figure 8: Mean power as a function of damping factor. Data are presented at $m^* = 10$ (\bullet), $m^* = 20$ ($*$), $m^* = 40$ (\blacktriangle), $m^* = 60$ ($+$) at $Re\ 165$ (a) with and (b) without the shedding term in equation 4. A reduction of maximum mean power can be observed when $m^* < 40$ with shedding while the maximum power is essentially independent of m^* when shedding is disregarded.

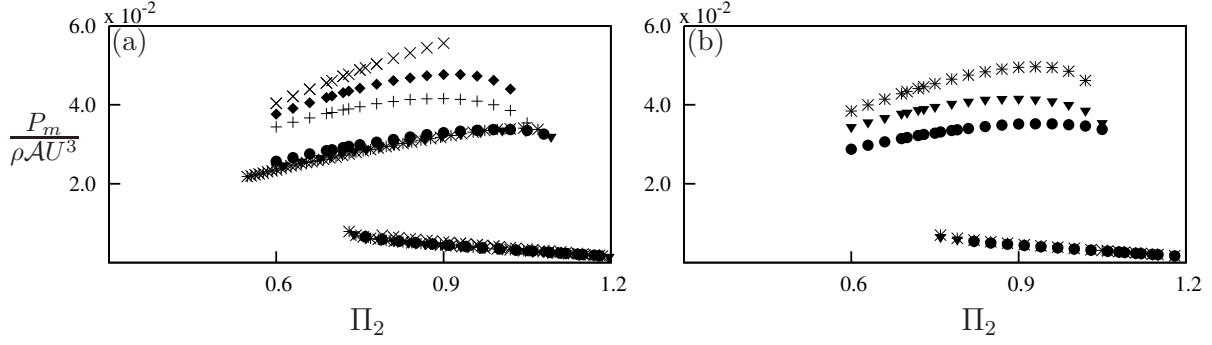


Figure 9: Mean power as a function of damping factor (a) with and (b) without the shedding term in equation 4. Data presented in both (a) and (b) were calculated using input data at $Re = 22300$ Parkinson and Smith (1964) where (a) shows mean power data at six different mass ratios: $m^* = 1$ (\times), $m^* = 5$ (\blacksquare), $m^* = 10$ ($+$), $m^* = 50$ (\bullet), $m^* = 100$ (\blacktriangledown) and $m^* = 1164$ ($*$) at $U^* = 175$. Data presented in (b) shows mean power data at three different reduced velocities: $U^* = 75$ (\bullet), $U^* = 175$ (\blacktriangledown) and $U^* = 375$ ($*$) at $m^* = 10$. The maximum mean power increases with decreasing m^* as well as increasing U^* at low m^* .

Π_1 cannot be ignored for cases where U^* is low.

The velocity time traces of example cases of both scenarios presented in figure 10 and 11 show that essentially the same phenomenon occurs in both cases whereby the velocity signal tends to shift from a sinusoidal signal towards a square wave. The corresponding displacement signal tends to become more like a triangular wave. When the inertia of the system reduces, the body can accelerate faster thus attaining higher velocities more rapidly and spend a higher proportion of the period at a high velocity. Higher velocities are favourable because they result in higher hydrodynamic forcing and power output from mechanical damping. However, the velocity is limited by the characteristics of the hydrodynamic forcing which reaches a maximum and then decreases past an incident angle of 13.21° which corresponds to a transverse velocity of $\dot{y}/U = 0.235$. It is estimated that the efficiency limit i.e ($U^* \rightarrow \infty$, $m^* \rightarrow 0$ and $\Pi_2 = 1.22$) will approach 13.5% which corresponds to a square wave velocity signal with a velocity amplitude that results in maximum hydrodynamic forcing.

3.5. Comparison with FSI simulations

As the results to this point are based on solving equations which come from the quasistatic assumption, it is natural to query how these results compare to the real flow. Here, results are presented of full fluid-structure direct numerical simulations (FSI) at $Re = 165$ and compared to the results obtained from the quasistatic model (QSS) at the same Re .

Qualitatively, the two compare very well. Similar trends were captured for both displacement and velocity amplitudes between QSS and FSI simulations as shown in figures 12(a) and 12(b). However, there is a reasonably large quantitative discrepancy (average of 30%) between QSS and FSI data, with the QSS model overpredicting the response of the body. Therefore the predicted power output is reduced in the FSI data, as shown in figure

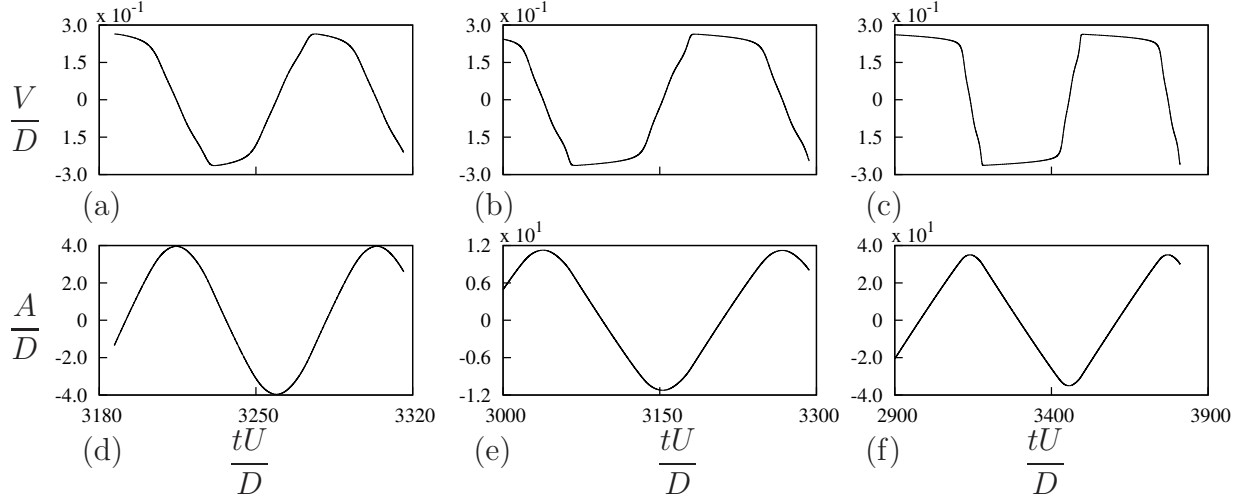


Figure 10: Time histories of displacement and velocity at $Re=22300$, $U^*=175$ and $\Pi_2 = 9.3 \times 10^{-1}$. The velocity time histories are presented for: (a) $m^* = 1164$; (b) $m^* = 10$; (c) $m^* = 5$. The time histories of displacement are presented for: (d) $m^* = 1164$; (e) $m^* = 10$; (f) $m^* = 5$. As the mass ratio decreases the velocity signal tend to transform from a sinusoidal towards a square signal and the displacement signal tend to move towards a triangular signal due to reduction in inertia.

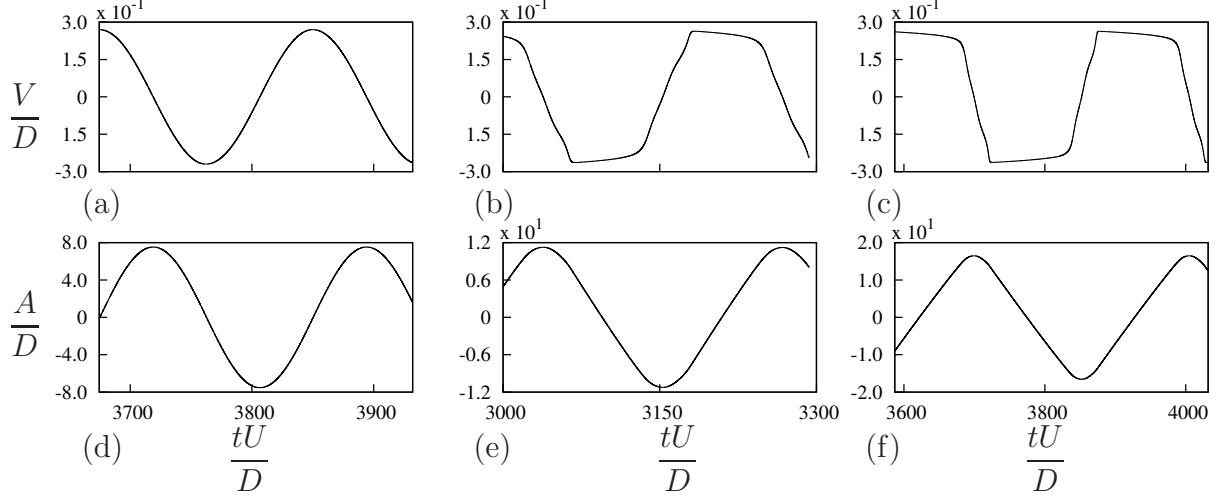


Figure 11: Time histories of displacement and velocity at $Re=22300$, $m^* = 10$ and $\Pi_2 = 9.3 \times 10^{-1}$. The velocity time histories are presented for: (a) $U^*=75$; (b) $U^*=175$ (c) $U^*=375$. The time histories of displacement are presented for: (d) $U^*=75$; (e) $U^*=175$; (f) $U^*=375$. As the mass ratio decreases the velocity signal tend to transform from a sinusoidal towards a square signal and the displacement signal tend to move towards a triangular signal.

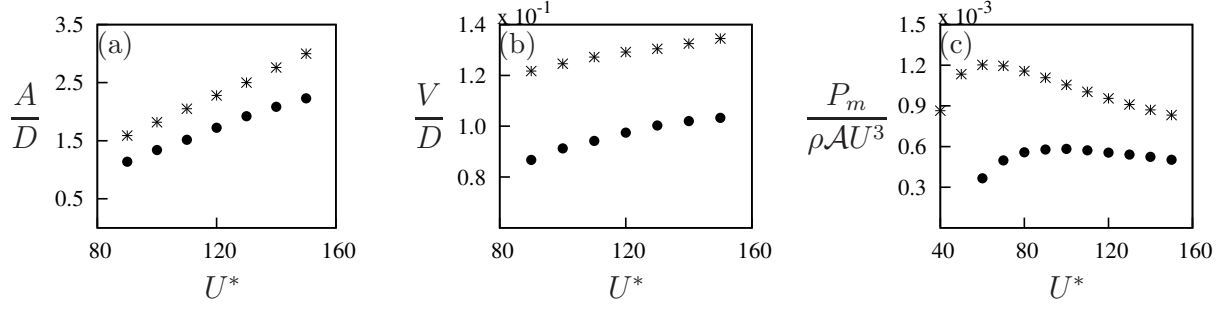


Figure 12: Comparison of data generated using the quasi-static theory (*) and full DNS simulations (●). (a) Displacement amplitude, (b) velocity amplitude and (c) mean power as functions of U^* . Data were obtained at $Re = 165$ and $\zeta = 0.075$. An average difference of 34% is observed for both displacement and velocity amplitude. However, the essential physics i.e the rise and fall of mean power, is captured by DNS simulations.

12(c). However, the FSI data does produce the main rise and fall of mean power when U^* was increased.

The exact reason behind this discrepancy is unclear. A possible explanation is that galloping is reasonably weak at $Re = 165$. It was reported by Barrero-Gil et al. (2009) that galloping only starts to occur at $Re \geq 159$. It may be that simulations conducted so close to the threshold for the onset of galloping are very sensitive to errors due to blockage or under-resolution, both of which can change the effective Re of the flow. Small changes in effective Re can have a significant impact on the fluid damping, and therefore on the amplitude and transverse velocity of the body. As power is a function of $(\dot{y})^2$ the error between QSS and FSI power is compounded.

4. Conclusion

In this paper, the power transfer of a square body under aero elastic galloping is analysed by solving the quasi-steady state model equations through numerical integration. At higher m^* ($m^* > 30$ at lower Re and $m^* > 50$ at high Re) the power output of the system is not dependent on U^* or natural frequency of the system, but controlled by the non-dimensionalised mass-damping constant Π_2 . By analysing key regions of the power vs U^* curve it is concluded that in order to obtain an optimum power output, the mass-damping constant Γ_2 should be high, but not so excessive that it hinders the galloping from reaching induced angles of attack where the forcing is significant. The effect of mass ratio was also observed. The peak efficiency was found to be 0.26% for $Re = 165$ and 6.7% for $Re = 22300$ when $\Gamma_2 = 0.314$ and $\Gamma_2 = 1.04$ respectively. In the low Re case, the mean power tends to decrease at $m^* < 30$ which appears to be due to the influence of vortex shedding. At $Re = 22300$ the opposite is observed where the mean power tends to increase with decreasing mass ratio, as well as the mean power increasing with increasing U^* at low mass ratios. For this higher Re case, When the mass ratio decreases, due to the lower inertia the velocity time trace tends to move from a sinusoidal signal towards a square signal where it sustains high velocities for longer periods of time which leads to a higher mean

power output. The limit to peak efficiency was found out to be 13.5% and occurs when $m^* \rightarrow 0$ and $U^* \rightarrow \infty$ and $\Pi_2 = 1.22$ by analysing the data trend by lowering the m^* .

- Barrero-Gil, A., Alonso, G., Sanz-Andres, A., Jul. 2010. Energy harvesting from transverse galloping. *Journal of Sound and Vibration* 329 (14), 2873–2883.
- Barrero-Gil, A., Sanz-Andrés, A., Roura, M., Oct. 2009. Transverse galloping at low Reynolds numbers. *Journal of Fluids and Structures* 25 (7), 1236–1242.
- Bernitsas, M. M., Raghavan, K., Ben-Simon, Y., Garcia, E. M. H., 2008. VIVACE (Vortex Induced Vibration Aquatic Clean Energy): A new concept in generation of clean and renewable energy from fluid flow. *Journal of Offshore Mechanics and Arctic Engineering* 130 (4), 041101–15.
- Den Hartog, J. P., 1956. *Mechanical Vibrations*. Dover Books on Engineering. Dover Publications.
- Glauert, H., 1919. The rotation of an aerofoil about a fixed axis. Tech. rep., Advisory Committee on Aeronautics R and M 595. HMSO, London.
- Griffith, M. D., Leontini, J. S., Thompson, M. C., Hourigan, K., 2011. Vortex shedding and three-dimensional behaviour of flow past a cylinder confined in a channel. *Journal of Fluids and Structures* 27 (5-6), 855–860.
- Joly, A., Etienne, S., Pelletier, D., Jan. 2012. Galloping of square cylinders in cross-flow at low Reynolds numbers. *Journal of Fluids and Structures* 28, 232–243.
- Lee, J., Bernitsas, M., Nov. 2011. High-damping, high-Reynolds VIV tests for energy harnessing using the VIVACE converter. *Ocean Engineering* 38 (16), 1697–1712.
- Leontini, J. S., Lo Jacono, D., Thompson, M. C., Nov. 2011. A numerical study of an inline oscillating cylinder in a free stream. *Journal of Fluid Mechanics* 688, 551–568.
- Leontini, J. S., Thompson, M. C., 2013. Vortex-induced vibrations of a diamond cross-section: Sensitivity to corner sharpness. *Journal of Fluids and Structures* 39, 371–390.
- Leontini, J. S., Thompson, M. C., Hourigan, K., Apr. 2007. Three-dimensional transition in the wake of a transversely oscillating cylinder. *Journal of Fluid Mechanics* 577, 79.
- Lighthill, J., 1986. Fundamentals concerning wave loading on offshore structures. *Journal of Fluid Mechanics* 173, 667–681.
- Luo, S., Chew, Y., Ng, Y., Aug. 2003. Hysteresis phenomenon in the galloping oscillation of a square cylinder. *Journal of Fluids and Structures* 18 (1), 103–118.
- Ng, Y., Luo, S., Chew, Y., Jan. 2005. On using high-order polynomial curve fits in the quasi-steady theory for square-cylinder galloping. *Journal of Fluids and Structures* 20 (1), 141–146.
- Païdoussis, M., Price, S., de Langre, E., 2010. *Fluid-Structure Interactions : Cross-Flow-Induced Instabilities*. Cambridge University Press.

- Parkinson, G. V., Smith, J. D., 1964. The square prism as an aeroelastic non-linear oscillator. *The Quarterly Journal of Mechanics and Applied Mathematics* 17 (2), 225–239.
- Raghavan, K., Bernitsas, M., Apr. 2011. Experimental investigation of Reynolds number effect on vortex induced vibration of rigid circular cylinder on elastic supports. *Ocean Engineering* 38 (5-6), 719–731.
- Raghavan, K., Bernitsas, M. M., Maroulis, D. E., 2009. Effect of Bottom Boundary on VIV for Energy Harnessing at $8 \times 10^3 < Re < 1.5 \times 10^5$. *Journal of Offshore Mechanics and Arctic Engineering* 131 (3), 031102.
- Sheard, G. J., Fitzgerald, M. J., Ryan, K., Jun. 2009. Cylinders with square cross-section: wake instabilities with incidence angle variation. *Journal of Fluid Mechanics* 630, 43.
- Thompson, M., Hourigan, K., Sheridan, J., Feb. 1996. Three-dimensional instabilities in the wake of a circular cylinder. *Experimental Thermal and Fluid Science* 12 (2), 190–196.
- Thompson, M. C., Hourigan, K., Cheung, A., Leweke, T., Nov. 2006. Hydrodynamics of a particle impact on a wall. *Applied Mathematical Modelling* 30 (11), 1356–1369.
- Tong, X., Luo, S., Khoo, B., Oct. 2008. Transition phenomena in the wake of an inclined square cylinder. *Journal of Fluids and Structures* 24 (7), 994–1005.
- Vio, G., Dimitriadis, G., Cooper, J., Oct. 2007. Bifurcation analysis and limit cycle oscillation amplitude prediction methods applied to the aeroelastic galloping problem. *Journal of Fluids and Structures* 23 (7), 983–1011.